THE JOURNAL OF PHYSICAL CHEMISTRY C

ACS AUTHORCHOICE

pubs.acs.org/JPCC Article

On the Optical Properties of Ag−Au Colloidal Alloys Pulsed Laser Ablated in Liquid: Experiments and Theory

Enza Fazio, Rosalba Saija, Marco Santoro, Saidi Abir, Fortunato Neri, Matteo Tommasini, and Paolo Maria Ossi*

Cite This: J. Phys. Chem. C 2020, 124, 24930−24939

Read Online

ACCESS | Metrics & More | Article Recommendations

ABSTRACT: We simulated the extinction spectra of Ag−Au alloyed nanoparticles produced by pulsed laser ablation in liquid of elemental targets followed by re-irradiation of suitable mixtures of the obtained colloidal suspensions. When we make use of the optical constants of Ag−Au alloys, our theoretical approach, developed in the framework of the T-matrix formalism, accurately reproduces the experimental features of the extinction spectra of laser-produced nanoalloys with compositions that span the entire composition range ($Ag_{25}Au_{75}$, $Ag_{50}Au_{50}$, and $Ag_{75}Au_{25}$).

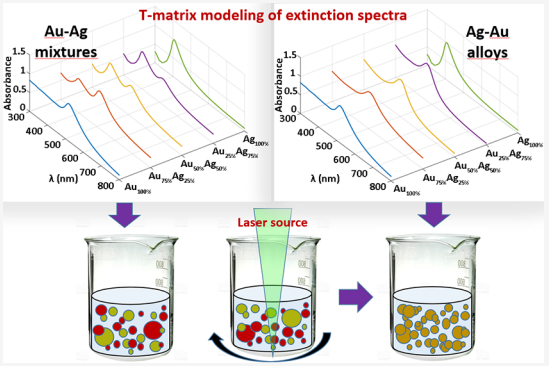

INTRODUCTION

Twenty years ago, plasmonics was introduced and defined as the discipline that deals with surface plasmon resonance (SPR)-related science and technology. A surface plasmon (SP) results from the coexistence of free electrons and photons in a single elementary excitation at the interface between a metal and a dielectric. The hybrid electric-photonic nature of plasmons allows one to control photons at the nanoscale. Plasmonics showed to be useful for quite different applications, such as, e.g., optical sensing[1] and phototherapy.[2] This is concomitant with the widespread choice of Ag and Au as the metals used to engineer a variety of progressively more elaborated surface nanostructures with SPR in the visible−near-IR region.

The artificial surface roughening at the nanometer scale of a noble metal is crucial as it determines the SP wavelength, intensity, and the full width at half-maximum (FWHM). Much attention was and still is devoted to design the shape of the surface nanostructures with optimal plasmonic performances geared toward specific applications. The main focus is on a wide tunability of the SPR associated to the controlled synthesis of the primary building blocks that support the plasmonic behavior. Several strategies have been adopted to this aim. Without any claim of completeness, among the lines of attack of the problem, we mention the efforts to synthesize Au nanorods by controlled chemical procedures (e.g., use of surfactants and proper seed growth approaches[3]), and the various approaches to produce periodic arrays of plasmonic nanostructures for chemical sensing applications.[4,5] Other strategies start with the controlled production of non-plasmonic nanostructures (e.g., silicon nanowires[6]) to subsequently decorate them with noble metals that impart the desired plasmonic properties.[7] Finally, we mention laser-based methods by which one can deposit on an inert support arrays of mutually assembled nanoparticles (NPs) previously synthesized in an expanding plasma plume.[8,9] Alternatively, by pulsed laser ablation in liquid (PLAL), one may directly obtain colloidal suspensions of noble metals[10,11] that can be sprayed on the support, forming a carpet of NPs.[12]

Extensive research was conducted on Ag, Au, and Ag−Au colloids, motivated by the concomitant intrinsic simplicity of the binary phase diagram of such a system and by its recognized wide potentiality for plasmonic applications. Several facts relevant to our discussion were assessed from experiments conducted in the past. During the exposition to laser irradiation of mixtures of elemental colloids, along the irradiation time an intermediate phase that consists of mutually contacting Ag and Au NPs develops and it precedes the formation of AgAu alloy NPs.[13] During PLAL in water, the early stages of the alloying process involve the formation of NPs organized as Au (core)−Ag (shell) structures.[13,14] The

Received: June 10, 2020
Revised: October 1, 2020
Published: October 28, 2020

https://dx.doi.org/10.1021/acs.jpcc.0c05270
J. Phys. Chem. C 2020, 124, 24930−24939

absorption peak of the laser-generated AgAu alloy lies between the plasmon peaks of elemental Ag and Au NPs;[15,16] the wavelength corresponding to the peak maximum depends on the constituent ratio in the alloy;[15,16] the irradiation time necessary to obtain Ag−Au alloys directly depends on the laser energy density.[15] With visible pulses (532 nm), both picosecond and nanosecond, the nonlinear optical response of the alloy NPs show a strong saturable absorption behavior.[16] When femtosecond pulses are used, with specific attention to control the nanoalloy oxidation resistance via an increase of Au content in the NPs, a threshold Au fraction is found beyond which the release of toxic Ag^+ in solution is quenched.[17]

Usually, to understand the structure and the kinetics of particles' formation *ad hoc* semi-empirical methods were adopted to best fit the optical properties of colloidal solutions subjected to progressive irradiation with laser beams.[18,19] Irrespective of the satisfactory results often obtained by these modeling approaches, such procedures are not sensitive to the changes that take place in the band structures of the constituents forming the final compound. More recently, some researchers have faced the problem proposing some model optical constants for noble metal alloys, which provide a realistic optical behavior not only in the region near the onset of interband transitions but also in the near-IR region.[19−21]

In this work, we carefully determine the optical response in the UV−Vis range of some colloidal Ag−Au solutions, obtained through a laser ablation process with controlled parameters, applying the transition matrix approach of the full scattering theory based on the analytic solution of the Maxwell equations.[22] This way, as long as the particles formed in the experiment can be considered as spherical monomers (possibly aggregated), we can understand with no ambiguity whether from the peculiar shape of the UV−Vis spectra of nanocomposites can be extracted information related to the effective formation of a metal alloy.

In addition, our theoretical approach, once fed by the appropriate optical constants, allows a reliable design of the SPR of the NPs that constitute the colloids according to the main process parameters, namely, the composition of the Ag−Au mechanical mixture leading to the alloy and the NP average size.

METHODS

Optical Cross Sections in the Framework of T-Matrix Approach. We recall here the essentials of the propagation of light through a low-density dispersion of anisotropic particles and the relations between measurable and computed quantities. In particular, we are interested in three cases: the spherical homogeneous scatterer, the radially non-homogeneous sphere, and the anisotropic scatterer made of clusters of non-identical spheres. In a homogeneous medium of refractive index n, the scattered electromagnetic field with η polarization that propagates in the direction $\boldsymbol{u}_{I\eta}$ with propagation constant $\boldsymbol{k}_I = nk_v\boldsymbol{u}_{I\eta}$, referred to the wavevector of vacuum $k_v = \omega/c$, takes on the asymptotic form $\boldsymbol{E}_S = E_0(e^{ink_v r}/r)\boldsymbol{f}(\boldsymbol{k}_S, \boldsymbol{k}_I)$. In this equation, $\boldsymbol{k}_S$ is the propagation direction of the scattered waves. The vector function $\boldsymbol{f}$, transverse to the direction of observation, is the normalized scattering amplitude: its vector nature gives a correct description of the state of polarization of the scattered wave. For particles of any shape, the scattering amplitude depends both on the direction of propagation of the incident wave, $\boldsymbol{k}_I$, and on the direction of observation, $\boldsymbol{k}_S$. Through the very definition of the vector function $\boldsymbol{f}$, the scattering, extinction, and absorption cross sections are defined as follows

$$C_{sca} = \int |\boldsymbol{f}(\boldsymbol{k}_S, \boldsymbol{k}_I)|^2 d\Omega$$

$$C_{ext} = \frac{4\pi}{nk}\Im[\boldsymbol{u}_{I\eta}\cdot\boldsymbol{f}(\boldsymbol{k}_S = \boldsymbol{k}_I, \boldsymbol{k}_I)]$$

$$C_{abs} = C_{ext} - C_{sca} \quad (1)$$

These relations show that the normalized scattering amplitude is the key quantity to describe the optical behaviour of micro- and nanoparticles in the far field.

The actual calculation of $\boldsymbol{E}_S$ and $\boldsymbol{f}$ relies on the imposition in the near field of the boundary conditions across the surface of the particle. To solve this problem, Waterman[23] devised a matrix formulation of electromagnetic scattering: the transition matrix method (T-matrix). Hereafter, we summarize the essentials of the T-matrix method, with emphasis on the relation between the transition matrix elements and the components of the scattering amplitude.[22] The starting point of the method is the expansion of $\boldsymbol{E}_I$, $\boldsymbol{E}_S$, and $\boldsymbol{E}_T$ (incident, scattered, and transmitted fields) in terms of a complete set of vector solutions of the Helmholtz equation. A suitable basis for the expansion is the set of vector spherical multipole fields $\boldsymbol{X}_{lm}(\hat{r})$, *i.e.*, the vector solutions of the Maxwell equations in a homogeneous medium, which are simultaneous eigenfunctions of the square of the radiation angular momentum (with eigenvalue $l(l+1)$) and its z component (with eigenvalue m) as well as the parity.[24] If we take into proper account the polarization of the field marked through the η index, the expansions of the incident $\boldsymbol{E}_{I\eta}(r)$ and the scattered $\boldsymbol{E}_{S\eta}(r)$ fields, respectively, result in

$$\boldsymbol{E}_{I\eta}(r) = \sum_{plm} \boldsymbol{J}_{lm}^{(p)}(r, nk) W_{lm}^{(p)}(\boldsymbol{u}_{I\eta}, \boldsymbol{k}_I)$$

$$\boldsymbol{E}_{S\eta}(r) = \sum_{plm} \boldsymbol{H}_{lm}^{(p)}(r, nk)\, A_{lm}^{(p)} \quad (2)$$

The $\boldsymbol{J}$ and $\boldsymbol{H}$ fields are divergence-free vector multipole fields and form a complete orthonormal set on the surface of a reference unit sphere. The superscript p attached to $\boldsymbol{J}$ and $\boldsymbol{H}$ is an index that distinguishes the magnetic multipole fields, $\boldsymbol{J}_{lm}^{(1)} = j_l(kr)\boldsymbol{X}_{lm}(\hat{r})$ and $\boldsymbol{H}_{lm}^{(1)} = h_l(kr)\boldsymbol{X}_{lm}(\hat{r})$, from the electric ones , $\boldsymbol{J}_{lm}^{(2)} = \frac{1}{k_v}\nabla\times\boldsymbol{J}_{lm}^{(1)}$ and $\boldsymbol{H}_{lm}^{(2)} = \frac{1}{k_v}\nabla\times\boldsymbol{H}_{lm}^{(1)}$. The $\boldsymbol{J}$ fields are described through Bessel functions, $j_l(kr)$,[24] and are regular at the origin, the $\boldsymbol{H}$ fields are defined through first-kind Hankel functions, $h_l(kr)$,[24] and satisfy the radiation condition, that is, when r tends to infinity, the fields should tend to 0 with at least r^{-1} dependence. Also, the transmitted field $\boldsymbol{E}_{T\eta}(r)$ must be regular at the origin, and its expansion can be taken in the form

$$\boldsymbol{E}_{T\eta}(r) = E_0 \sum_{plm} \boldsymbol{J}_{lm}^{(p)}(\boldsymbol{r}, k_0)\, C_{\eta lm}^{(p)} \quad (3)$$

where $k_0 = n_0 k_v$, with n_0 the refractive index of the scatterer and k_v the wavevector in vacuum. Owing to the linearity of the Maxwell equations and the boundary conditions across the surface of the particle, we can find the relation between the known amplitudes of the incident field, $W_{lm}^{(p)}(\boldsymbol{u}_{I\eta}, \boldsymbol{k}_I)$, and the unknown amplitudes of the scattered fields, $A_{lm}^{(p)}(\boldsymbol{u}_{I\eta}, \boldsymbol{k}_I)$

$$A_{\eta lm}^{(p)} = \sum_{p'l'm'} S_{lm,l'm'}^{(p,p')} W_{l'm'}^{(p')}(\boldsymbol{u}_{I\eta}, \boldsymbol{k}_I) \quad (4)$$

https://dx.doi.org/10.1021/acs.jpcc.0c05270
J. Phys. Chem. C 2020, 124, 24930−24939

The quantities $S^{(p,\,p')}_{lm,\,l'm'}$ are the elements of the transition matrix and contain all the information about the scattering process through which the particle transforms the incident wave into the scattered wave. For large values of r, *i.e.*, in the far field, where we can use the asymptotic form of the $\boldsymbol{H}$ multipole fields, we can express the matrix elements of the normalized scattering amplitude in terms of the transition matrix elements

$$-f_{\eta,\eta'} = \frac{i}{4\pi k}\sum_{plm} W^{(p)*}_{lm}(\boldsymbol{u}_{S\eta}, \boldsymbol{k}_S)A^{(p)}_{\eta lm} = \frac{i}{4\pi k}\sum_{plm}\sum_{p'l'm'} W^{(p)*}_{lm}(\boldsymbol{u}_{S\eta}, \boldsymbol{k}_S)S^{(p,p')}_{lm,l'm'}W^{(p')}_{l'm'}(\boldsymbol{u}_{I\eta}, \boldsymbol{k}_I) \tag{5}$$

where the symbol * indicates the complex conjugate.

Homogeneous Sphere. The computation of the transition matrix elements, the kernel quantities through which the particle optical properties can be derived, is easily performed when we consider homogeneous spheres. Due to symmetry, the only non-vanishing elements of T-matrix are those on the diagonal. These elements can be analytically calculated by imposing the continuity conditions of the electromagnetic fields at the surface of the sphere, *i.e.*, with ρ the radius of the sphere, for $r = \rho$. With this straightforward procedure, we determine these quantities that match the well-known Mie scattering coefficients[25] a_l and b_l:

$$-S^{(1)}_l = b_l = \frac{\frac{n}{n_0}[k\rho j_l(k\rho)][k_v r j_l(k_v r)]'_{r=\rho} - [k_v\rho j_l(k_v\rho)][krj_l(kr)]'_{r=\rho}}{\frac{n}{n_0}[k\rho h_l(k\rho)][k_v r j_l(k_v r)]'_{r=\rho} - [k_v\rho j_l(k_v\rho)][krh_l(kr)]'_{r=\rho}}$$

$$-S^{(2)}_l = a_l = \frac{[k\rho j_l(k\rho)][k_v r j_l(k_v r)]'_{r=\rho} - \frac{n}{n_0}[k_v\rho j_l(k_v\rho)][krj_l(kr)]'_{r=\rho}}{[k\rho h_l(k\rho)][k_v r j_l(k_v r)]'_{r=\rho} - \frac{n}{n_0}[k_v\rho j_l(k_v\rho)][krh_l(kr)]'_{r=\rho}} \tag{6}$$

In eq 6 the sign (′) states the first derivative of the functions. $S^{(1,2)}_l$ are the quantities that enter in eq 1 and allow us to calculate the optical cross section.

Radially Non-homogeneous Sphere. For a radially non-homogeneous sphere, we have to reformulate the expansion of the transmitted field $\boldsymbol{E}_{T\eta}$ considering two relevant questions. First, when the refractive index is space-dependent, the electric and the magnetic field do not separately satisfy the Helmholtz equations. Instead, we are in the presence of a coupled system due to the assumed inhomogeneity of the medium. Moreover the $\boldsymbol{J}$-multipole fields, defined through Bessel functions, now are no more suitable to describe the propagation in a medium with $n_0 = n_0(r)$, which is a regular function of the distance from the center. Therefore, we assume that the electric and the magnetic field can be expanded as

$$\boldsymbol{E}_{T\eta} = E_0\sum_{\eta lm}\left[C^{(1)}_{\eta lm}\phi_l(r)\boldsymbol{X}_{lm}(\hat{r}) + C^{(2)}_{\eta lm}\frac{1}{n_0^2}\frac{1}{k_v}\nabla\times\psi_l(r)\boldsymbol{X}_{lm}(\hat{r})\right]$$

$$\boldsymbol{B}_{T\eta} = E_0\sum_{\eta lm}\left[C^{(1)}_{\eta lm}\frac{1}{k_v}\nabla\times\phi_l(r)\boldsymbol{X}_{lm}(\hat{r}) + C^{(2)}_{\eta lm}\psi_l(r)\boldsymbol{X}_{lm}(\hat{r})\right] \tag{7}$$

Here, $\phi_l(r)$ and $\psi_l(r)$, which, for the homogenous sphere, are simply Bessel functions, are radial functions satisfying a suitable differential equation.[22] Also in this case, once we apply the boundary conditions, the T-matrix is diagonal and the non-vanishing elements are

$$-S^{(p)}_l = \frac{[G^{(p)}_l(kr)]'_{r=\rho}k\rho j_l(k\rho) - \left(1+\frac{n_0}{n}\delta_{p2}\right)^2 G^{(p)}_l(k\rho)[krj_l(kr)]'_{r=\rho}}{[G^{(p)}_l(kr)]'_{r=\rho}k\rho h_l(k\rho) - \left(1+\frac{n_0}{n}\delta_{p2}\right)^2 G^{(p)}_l(k\rho)[krh_l(kr)]'_{r=\rho}} \tag{8}$$

where $G^{(1)}_l(kr) = kr\phi_l(kr)$ and $G^{(2)}_l(kr) = kr\psi_l(kr)$. Taking into account these observations, from this point on, the calculation of the optical cross section proceeds as described above.

Cluster of Spheres. In the case of a non-spherical particle made of an aggregate of N spheres,[26] we have to consider that the field scattered by the aggregate as a whole is given by a superposition of the scattered fields originated by the spheres that constitute the cluster

$$\boldsymbol{E}_{S\eta} = \sum_{\alpha}\sum_{plm}\boldsymbol{H}^{(p)}_{lm}(r_\alpha, n_\alpha k)A^{(p)}_{\alpha\eta lm} \tag{9}$$

where α is the index that identifies the sphere in the aggregate. The addition theorem for multipole fields allows us to refer the incident field $\boldsymbol{E}_{I\eta}$ to the center of each αth sphere; we can impose the boundary conditions across the surfaces obtaining the $A^{(p)}_{\alpha\eta lm}$ amplitudes. Since the transition matrix for the aggregate as a whole is defined with respect to a common origin, 0, we use once again the addition theorem to refer the α-multicentered fields to the same origin. Such an analytic procedure leads us to write the T-matrix elements as

$$-S^{(p,p')}_{lm,l'm'} = \sum_{\alpha\alpha'}\sum_{qlM,q'l'M'} I^{(pq)}_{0lm,\alpha LM}[M^{-1}]^{(qq')}_{\alpha LM,\alpha' L'M'}I^{(q'p')}_{\alpha' L'M',0l'm'} \tag{10}$$

where the matrix $\boldsymbol{M}$ takes into account the chemical and physical properties of the individual monomers, and the elements of matrices $\boldsymbol{I}_{0-a}$ and $\boldsymbol{I}_{a-0}$ perform the transfer between the different origins. The transition matrix approach has invaluable advantages when we deal with the properties of dispersions of particles for which the distribution of orientations is known. Because the transition matrix was obtained using radiation angular momentum eigenfunctions, it has well-defined transformation properties under rotation that allow a straightforward (analytical) evaluation of orientation averages.[27] Explicit formulas for the averages of quantities of practical interest, based on the application of rotation operators on the elements of T-matrix, can be found in refs 26, 28 for some cases of orientational distribution functions. Indeed, since we are interested in the optical properties of a dispersion as a whole, we exploit these properties assuming a random distribution of orientations. The accuracy of the solution obtained with an analytical evaluation of the averages is much improved and results in a remarkable lowering of calculation time[1].

EXPERIMENTAL METHODS

The irradiations were carried out for 20 min, with a Nd:YAG laser (New Wave Mod. Tempest 300) that provides 5 ns FWHM laser pulses at 532 nm wavelength. The laser fluence was 1.5 J cm^{-2} at a repetition rate of 10 Hz. A convex lens having focal length of 20 cm allowed focusing vertically the laser beam to the surface of the target that was immersed in distilled water. The re-irradiations were performed using the same laser source as for the synthesis, at the same wavelength, for 120 min at a laser fluence of 1.2 J cm^{-2}. Both elemental colloids and physical mixtures were exposed to re-irradiation with the same laser irradiation parameters. The samples, prepared by dropping the colloids onto a carbon-coated copper

https://dx.doi.org/10.1021/acs.jpcc.0c05270
J. Phys. Chem. C 2020, 124, 24930−24939

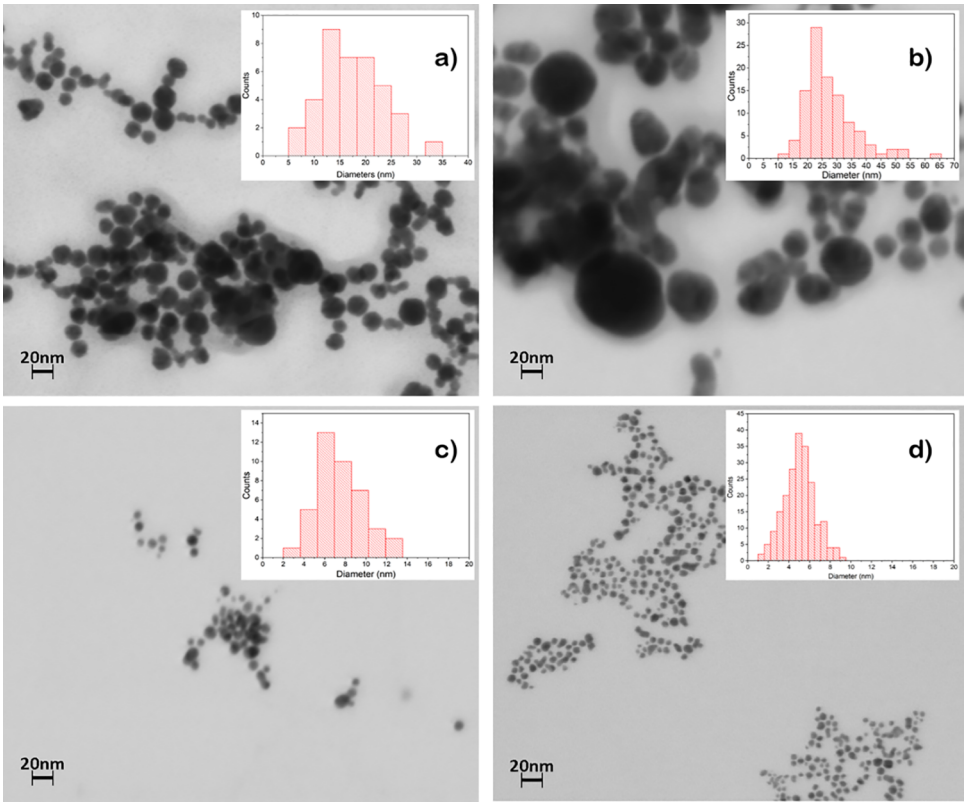

Figure 1. Elemental NPs prepared by PLAL at f = 10 Hz, t = 20 min, F = 1.5 J cm^{-2}: (a), e-Ag and (b), e-Au. Elemental NPs re-irradiated at f = 10 Hz, t = 120 min, F = 1.2 J cm^{-2}: (c), r-Ag and (d), r-Au (f is the laser repetition rate, F is the laser fluence, and t is the exposure time).

grid and allowing them to dry at room temperature, were characterized in size and shape using a scanning electron microscope (Zeiss-Merlin, equipped with a Gemini II column), operating in transmission mode (STEM) at an accelerating voltage of 30 kV. The SEM apparatus is coupled with a Quantax EDX spectrometer to carry out energy-dispersive X-ray (EDX) analysis. The EDX detected pear-shaped dimension is about 0.7 μm. We carried out also transmission electron microscopy (TEM) measurements with a JEOL JEM 2010 electron microscope (LaB 6 electron gun) operating at 200 kV. We performed a quantitative estimate of Ag, Au, and Ag−Au alloys concentration by graphite furnace atomic absorption spectroscopy (GF-AAS) using an atomic absorption spectrometer equipped with a single-element hollow cathode lamp and a programmable sample dispenser (PSD) autosampler. For the analysis, we diluted the samples 1:5000 (v:v) with 0.2% HNO_3 (AAS grade). The analytical method was validated according to the ICH (International Council for Harmonization of Technical Requirements for Pharmaceuticals for Human Use, 2005) guidelines. The linearity was better than 0.999, the precision expressed as a relative standard deviation resulted of 0.552, and a detection limit of 5.0 ng/mL. We measured the optical extinction spectra of the colloids with a Perkin-Elmer Lambda 750 UV−Vis spectrophotometer using a quartz cuvette with an optical path length of 1 cm.

RESULTS AND DISCUSSION

Synthesis and Characterization of Colloids. We synthesized by PLAL elemental colloidal suspensions of Ag and Au NPs, from now on referred to as e-Ag and e-Au. Freshly synthesized Ag and Au NPs appear spherical and, due to the deposition procedure, partly coalesced. From the size histogram, most of the particles are sized in the range 15−20 nm (e-Ag) and 25 nm (e-Au) (see Figure 1). We prepared physical mixtures of Ag and Au colloids taking selected volume fractions from the elemental colloids and mixing them. Both elemental colloids and physical mixtures were exposed to re-irradiation with the same laser irradiation parameters as for the synthesis. In the case of a physical mixture, with this prolonged re-irradiation time, it is likely that we induced NP formation of Ag−Au alloys.[15] The re-irradiation of the e-Ag and e-Au samples results in a reduced average NP size, down to about 6 nm for both metals (see Figure 1). The re-irradiated samples from here on are named r-Ag and r-Au.

Regarding the physical mixture of the e-Ag and e-Au NPs and of the re-irradiated NP mixture sample, in Figure 2a, we report a representative STEM morphology for the $Ag_{50}Au_{50}$ as-prepared mixture (from here on, m-$Ag_{50}Au_{50}$). The seeming reduced average NP size with respect to the pristine e-Ag and e-Au NPs can be explained considering our preparation method: since the liquid volumes are extracted with a pipette from the bulk of each elemental colloid, the biggest NPs are lacking from the mixture being precipitated at the bottom of the containers. In Figure 2b−g, we report a morphological and structural investigation of the re-irradiated $Ag_{50}Au_{50}$ NP mixture (from here on, r-$Ag_{50}Au_{50}$). The STEM pictures in panels (b) and (c) of Figure 2 indicate that irradiation does not significantly modify the morphology of the NP assemblies. Panel (f) of Figure 2 displays the lattice spacing measured in one of such crystalline particles. The value of 0.2205 nm is typical of crystalline Au NPs, in agreement with literature data.[29,30] The indexed rings in the SAED pattern, panel (g) of Figure 2, are characteristic of a crystalline fcc structure, as expected for a Ag−Au alloy.[31]

https://dx.doi.org/10.1021/acs.jpcc.0c05270
J. Phys. Chem. C 2020, 124, 24930−24939

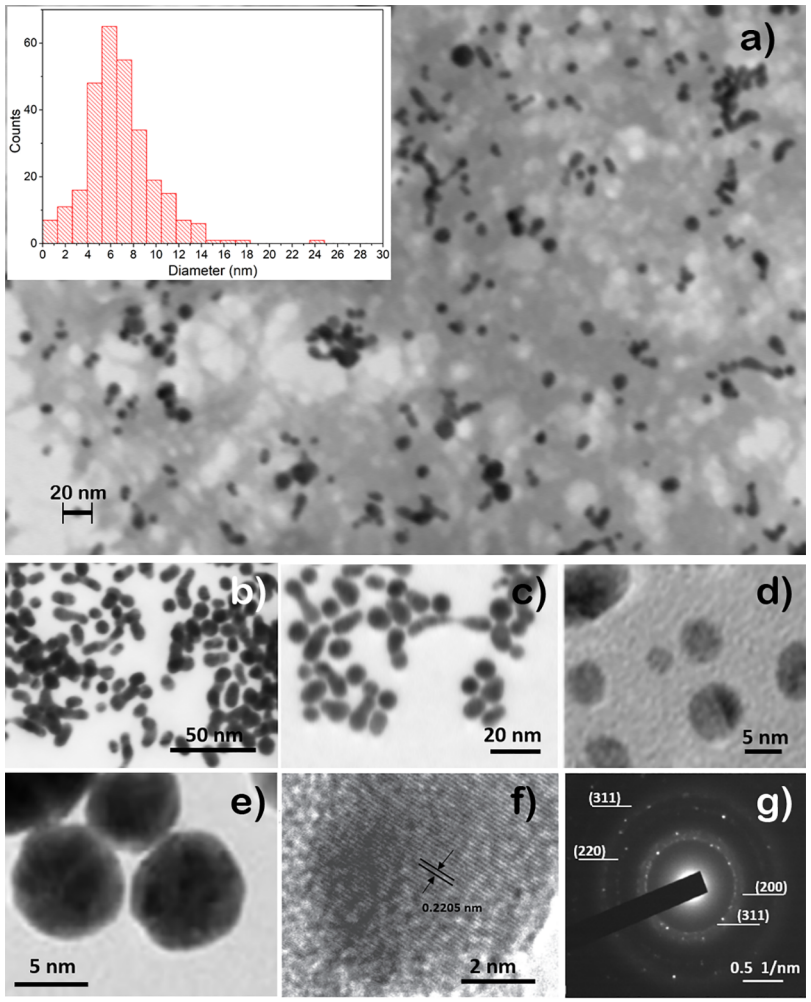

Figure 2. Representative morphology and size histogram of m-$Ag_{50}Au_{50}$ (physical mixture, panel (a)); typical morphology of r-$Ag_{50}Au_{50}$ (re-irradiated NP mixture, panels (b) and (c)); TEM high magnification pictures of selected NPs (panels (d) and (e)) and measured lattice spacing (panel (f)); SAED pattern (panel (g)) indexed according to the expected fcc structure of a Ag−Au alloy.

The EDX analysis of the selected different samples, $Ag_{75}Au_{25}$, $Ag_{50}Au_{50}$, and $Ag_{25}Au_{75}$ alloys, provided the atomic fraction of the species, expressed in percentage, as reported in Table 1.

Table 1. Concentration and Atomic Fractions for e-Ag, e-Au, and r-Ag_xAu_{100-x} Alloy NPs Obtained from GF-ASS and EDX Data, Respectively

sample	concentration (μg/mL)	Ag and Au fraction (at %)
e-Ag	168.8 ± 4.7	100.0−0.0
e-Au	230.4 ± 3.5	0.0−100.0
r-$Ag_{75}Au_{25}$	98.8 ± 1.6	66.1−33.9
r-$Ag_{50}Au_{50}$	128 ± 2.4	46.8−53.2
r-$Ag_{25}Au_{75}$	112.3 ± 1.7	22.7−77.3

Simulations of the Extinction Spectra. *Pure Metal Colloids (e-Ag and e-Au).* In Figure 3, we collect the optical properties of the elemental NPs as represented by the extinction spectra, both measured (red lines, experiment) and calculated (blue lines, theory). For as-prepared Ag NPs (e-Ag), a single peak centered at 407 nm with an FWHM of 70 nm is a marker of isolated, spherical particles (Figure 3a). Figure 3c shows the extinction spectrum of as-prepared Au NPs (e-Au), a single feature peaked at 526 nm, with an FWHM of about 80 nm. After the laser re-irradiation (120 min) for both metals, we observe a slight blue-shift of SPR (for Ag, from 407 down to 400 nm; for Au, from 526 to 522 nm). Particularly, the FWHM decreases to 55 nm for Ag and remains almost unchanged for Au (Figure 3d). In agreement with recent observations,[32−34] we conclude that re-irradiation with nanosecond laser pulses produces a consistent particle fragmentation in the colloids of both metals.

We now discuss the theoretical UV−Vis spectra obtained for two couples of elemental samples. The first couple mimics the as-prepared colloids in distilled water (e-Ag and e-Au). The second couple of samples consists of re-irradiated colloidal solutions (r-Ag and r-Au) for 120 min. The optical constants for both a Au NP and a Ag NP are those derived from the work of Johnson and Christy.[35] Since e-Ag and e-Au are polydispersed in size, in the limit of low dilution, we are confident that the optical properties of both elemental colloids can be determined through a weighted average of particles sizes, from r_{min} = 1 nm to r_{max} = 300 nm, of single particle extinction cross sections calculated as briefly reported in the preceding section

https://dx.doi.org/10.1021/acs.jpcc.0c05270
J. Phys. Chem. C 2020, 124, 24930−24939

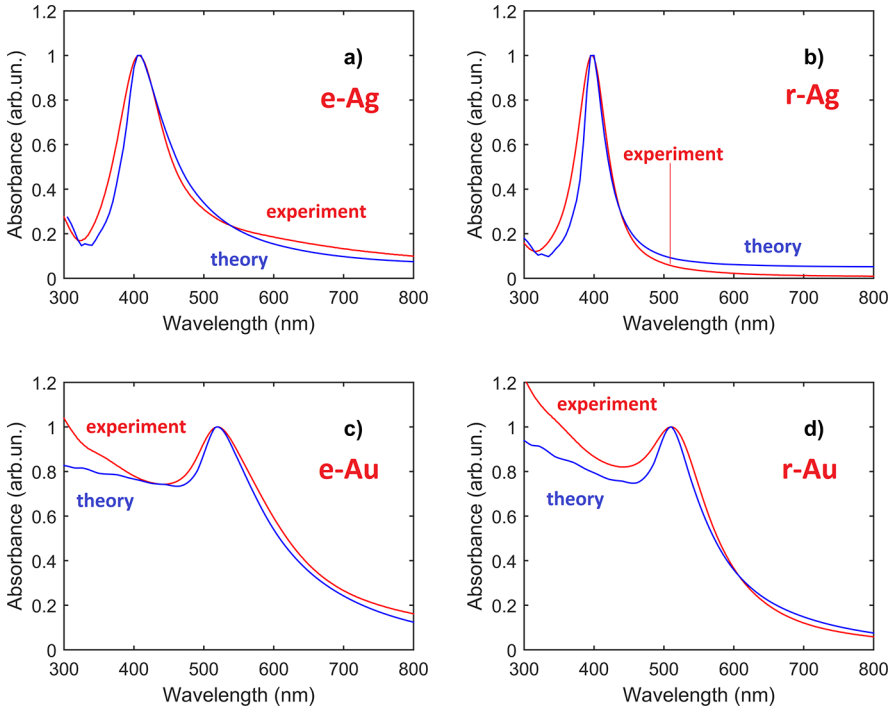

Figure 3. Extinction spectra of elemental NPs: Ag (as prepared, e-Ag panel (a); re-irradiated, r-Ag panel (b)), and Au (as prepared, e-Au panel (c); re-irradiated, r-Au panel (d)). In all panels, red curves, labeled experiment, refer to experimental data; blue curves, labeled theory, refer to best fits from theory, see Methods.

$$\langle \sigma_{ext} \rangle = \int_{r_{min}}^{r_{max}} dr\ n(r)\sigma_{ext}(r) \tag{11}$$

As suggested by the sampling in size, we choose a simple analytical function of the log normal type

$$n(r) \propto r^{-1} \exp\left[-\frac{(\ln r - \ln r_m)^2}{2(\ln \sigma_m)^2}\right] \tag{12}$$

to fit the experimental data. The results of the theoretical analysis are plotted together with the experimental spectra in Figure 3a,b for Ag NPs before and after the laser re-irradiation and in Figure 3c,d for Au NPs. From Figure 3 and Table 2,

Table 2. Values of the Parameters Obtained through the Best Fit Procedure of the Experimental Data Shown in Figure 3

	r_{av} (nm)	σ	r_{min} (nm)	r_{max} (nm)
e-Ag	30	1.5	1	300
r-Ag	25	1.3	1	300
e-Au	30	2	1	100
r-Au	15	2	1	100

where we report the best fit parameters obtained with the above-described theoretical procedure, we notice that the further fragmentation of the elemental NPs due to re-irradiation is confirmed by the accuracy of our theoretical computation. Overall, our best fits are in agreement with the experimental data for all elemental samples.

Mixtures of the Elemental Colloids. In Figure 4, we show the comparison between the UV−Vis spectra for the colloids of the equiatomic m-$Ag_{50}Au_{50}$ mixture and of their re-irradiated counterparts, r-$Ag_{50}Au_{50}$. The first curve (blue line, labeled m-$Ag_{50}Au_{50}$) displays two peaks, one centered at about

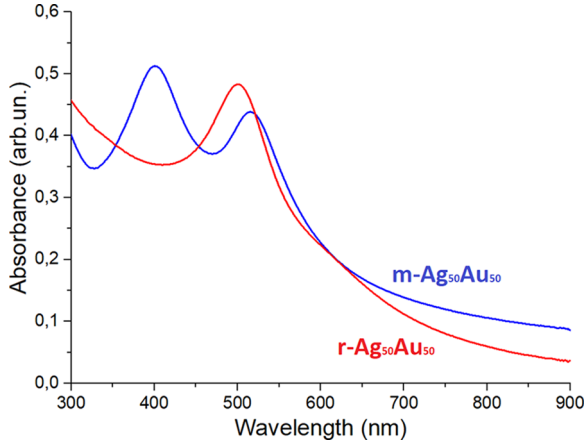

Figure 4. Extinction spectra of the initial $Ag_{50}Au_{50}$ equiatomic physical mixture (m-$Ag_{50}Au_{50}$) of the as-prepared colloids (blue line) and the re-irradiated colloids (r-$Ag_{50}Au_{50}$) (red line). Notice that the two features due to Ag and Au isolated, spherical NPs in m-$Ag_{50}Au_{50}$ reduce to a single feature in r-$Ag_{50}Au_{50}$, blue-shifted with respect to the SPR of the initial e-Au colloid.

398 nm (FWHM 48 nm), due to e-Ag NPs, the second at 511 nm (FWHM 35 nm), due to e-Au NPs. Even if the shape of both peaks indicates the presence of isolated, spherical NPs, the mixed sample shows new features as compared to the extinction spectra of the colloids in Figure 3. The SPR peaks are shifted toward lower wavelengths: from 407 to 398 nm for e-Ag and from 526 to 511 nm for e-Au. Peaks are also narrower: the FWHM changes from 70 to 48 nm for e-Ag and from 80 to 35 nm for e-Au. This led us to theoretically analyze the spectra of purely mixed samples to understand the nature of the above changes. The spectrum of the re-irradiated colloids (red line labeled r-$Ag_{50}Au_{50}$ in Figure 4) consists of a

https://dx.doi.org/10.1021/acs.jpcc.0c05270
J. Phys. Chem. C 2020, 124, 24930−24939

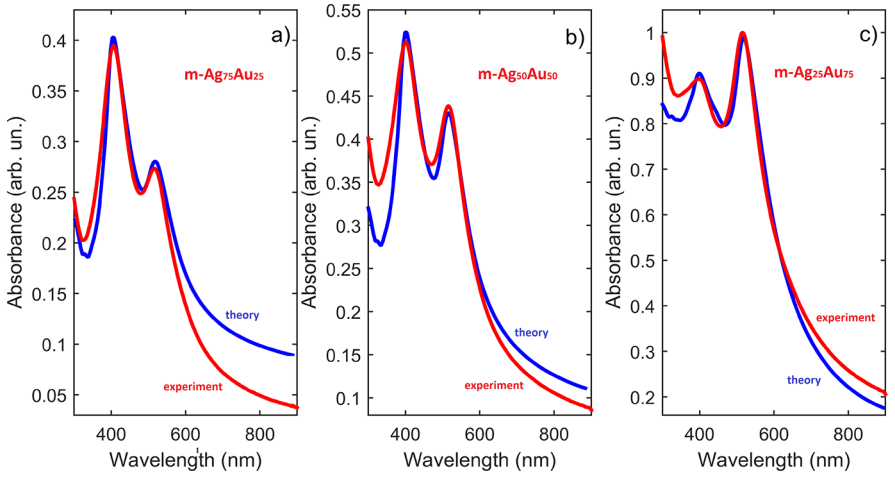

Figure 5. Extinction spectra from experiment (red line) and simulation (blue line) for three m-Ag_xAu_{100-x} mixed colloids of different stoichiometry, spanning the composition range: (a) m-$Ag_{75}Au_{2575}Au_{25}$; (b) m-$Ag_{50}Au_{50}$; (c) m-$Ag_{25}Au_{75}$.

single peak centered at 504 nm (FWHM of 52 nm). Thus, the optical signal from Ag NPs disappeared and the one from Au NPs is blue shifted and broadened, lying between those of e-Ag and e-Au.[15,16] Its displacement toward the Au feature is likely to indicate that the composition of the NPs is enriched in Au, similar to what was reported.[15,16] The result of the re-irradiation indicates that the NPs underwent a drastic change leading to the formation of a nanoalloy.[14,18,36]

In Figure 5, we report the UV−Vis and the simulated extinction spectra of m-Ag_xAu_{100-x} colloids for selected x values. The reported simulations make use of information on the average NP size as in Table 2.

Here, we notice further effects: (1) the relative intensity of the peak at about 400 nm, associated to Ag NPs, increases on increasing Ag content, (2) the Ag peak undergoes a gradual red shift from 398 to 406 nm, and (3) the Au NP feature shifts progressively from 515 to 507 nm on lowering the Au content. This is further confirmation that the surface plasmon characteristics of Ag and Au colloids strongly depend on the stoichiometric ratio of the mixture.[15,36] Electron microscopy images show that in the Au−Ag mixtures the NPs have a tendency to join together (see Figure 2a).

The observed shifts can be theoretically justified by supposing that, upon mixing, there is a weak interaction, due to nanoscale forces mainly of electrostatic nature,[37] between the particles that make up the mixture. This interaction, also studied from the experimental point of view,[36] is related to the high activity of Ag NPs that has been shown to depend on the wavelength of the laser radiation used in the synthesis.[36] Moreover, the change in broadening of plasmon band compared with that obtained for elemental colloids indicates the collective nature of the SPR of the mixed sample.[38] In the simulation, we focused on the electromagnetic interaction via the multiple scattering effects that come into play in the mixed sample. To take into account these effects, we calculate the optical properties (σ_{ext}) through the T-matrix approach, referring to the simplest form of aggregation: a dimer consisting of a Ag sphere and a Au sphere. By varying the distance between the monomers that make up such a binary system and by mediating over all the possible orientations, it was possible to take into account such shifts that are a fingerprint of multiple scattering interaction between the monomers that constitute the dimer. Another interesting aspect of the simulation shown in Figure 5, which also takes into account the size distribution of the particles (see Table 2), is that, as the concentration of gold NPs in the m-samples decreases, the optimum interaction distance increases going from about 5 nm (m-$Ag_{25}Au_{75}$) to about 10 nm (m-$Ag_{50}Au_{5050}Au_{50}$) to about 15 nm (m-$Ag_{75}Au_{25}$). This confirms that, in water, the more chemically stable Au NPs control the characteristics of the NP assembly and aggregation.[36]

Re-irradiated Mixtures of Elemental Colloids. Here, we present the simulations obtained for the re-irradiated samples made by mixing e-Au and e-Ag colloids, where the Ag fraction ranges from 25% to 75%. From the analysis of the experimental data (see Figure 4 for the equiatomic composition case), we observe the disappearance of the lowest frequency peak, which we previously assigned to Ag NPs. The question that arises is which chemical−physical process is responsible for this behavior. Experiment demonstrates that, in agreement with the assessed literature,[15,16] after the re-irradiation, particles with different optical properties to those of e-NPs were formed. We aim at demonstrating that our theoretical approach can discriminate whether such particles are as follows:

(1) core−shell NPs;
(2) NPs with optical properties that can be derived in terms of an effective dielectric constant following Bruggeman effective medium approximation (EMA);[39]
(3) a new kind of NPs, the optical properties of which can be simulated assuming that re-irradiation led to the formation of Ag−Au alloys. In this case, we consider two different models for the dielectric constant: the model of Rioux et al.,[20] which we refer as analytic model, and the model of Peña-Rodriguez et al.[21]

In Figure 6, we present the computed normalized absorption for different nanospheres with diameter r = 20 nm, compared with the experimental spectrum for the colloid r-$Ag_{50}Au_{50}$.

The curves are obtained for a core−shell spherical NP and for homogeneous spheres using both Bruggeman's EMA and dielectric optical constant coming from the analytic model.[20] The core−shell NP is constituted by a shell the volume of which is 50% of the total volume, and we consider both the case of Au (core) with Ag (shell) and Ag (core) with Au (shell). In the simulation, we adopted for Ag and Au the Johnson and Christy dielectric constants.[35] The Bruggeman's

https://dx.doi.org/10.1021/acs.jpcc.0c05270
J. Phys. Chem. C 2020, 124, 24930−24939

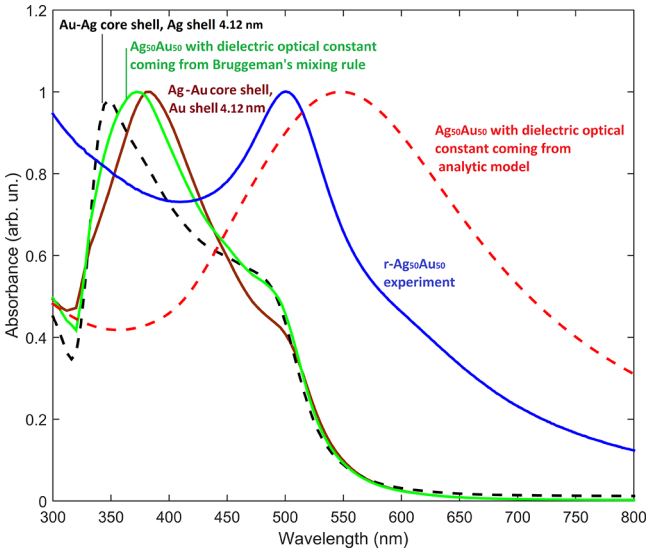

Figure 6. Extinction spectra for $Ag_{50}Au_{50}$, from different models: Au−Ag core shell, Au shell, 4.12 nm (red line); Au−Ag core shell, Ag shell, 4.12 nm (black dashed line); $Ag_{50}Au_{50}$ with dielectric optical constant coming from Bruggeman's mixing rule (green line); $Ag_{50}Au_{50}$ with dielectric optical constant coming from analytic model[20] (red dashed line); the blue line refers to the experimental extinction spectrum of r-$Ag_{50}Au_{50}$ colloids.

effective dielectric constant is derived for a mixture of 50% Ag and 50% Au. In Figure 6, we notice that the absorption spectra for the three above models (red and black dashed curves, green curve, and red dashed curve) are very far from the experimental data. As expected, in the first case, the layered structure introduces a further peak due to the presence of the core that marks the optical behavior. The Bruggeman's model gives an absorption spectrum with a behavior that is, as expected, an intermediate result between those of the two core-shell spectra. Also, the result obtained by Rioux's analytic model (red dashed curve) presented in Figure 6 is far from the experimental data. All such unsatisfactory results indicate that the re-irradiation of the sample results in colloids made of NPs with optical properties that can no longer be described through the dielectric functions that make use of a mixing rule based on Johnson and Christy results or on a multiparametric modification of Drude−Lorentz model. Indeed, any mixing rule ultimately tends to preserve the main physical characteristics of the noble metals used in the experiment. For these reasons, we resort to the optical constants for real Ag−Au alloys obtained from spectroscopic ellipsometry measurements on thin films fabricated by electron beam evaporation.[21] The ellipsometric spectra of thin films of Ag−Au alloys with different compositions were analyzed by an analytical procedure based on Kramers−Kronig (K-K) compliant cubic B-splines,[40] this way ensuring the physical meaning of the obtained complex dielectric function. A three-phase multilayer model was assumed in which the second layer, modeled as a Bruggeman's mixture of voids and Ag−Au islands, simulates the film surface with its roughness, lying between the ambient and the high-density region of the alloy film.[21] In Figure 7a and c, we display the values of the real (n) and imaginary (κ) parts of the refractive index corresponding to the r-Ag−Au alloys we prepared re-irradiating colloid mixtures containing (i) 25%Ag−75%Au (red line), (ii) 50%Ag−50%Au (blue line), and (iii) 75%Ag−25%Au (green line) together with the real

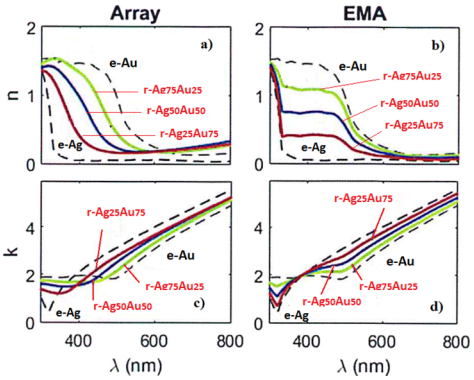

Figure 7. Real (n, panel (a)) and imaginary (κ, panel (c)) parts of the refractive index as functions of the wavelength for re-irradiated r-Ag-Au colloids of different compositions: red line, r-$Ag_{25}Au_{75}$; blue line, r-$Ag_{50}Au_{50}$; green line, $Ag_{75}Au_{25}$; data for pure Ag and Au (e-Ag and e-Au) are reported. In panels (b) and (d), same as in panels (a) and (c), calculated from Bruggeman's mixing rule.

and imaginary parts of the refractive index of the pure noble metals.[35] For comparison in Figure 7b and d, we show the values of n and κ obtained with the Bruggeman's mixing rule for the same systems.

We remark a couple of peculiarities in the trend of the refractive index as a function of the wavelength as the composition changes: first, for the alloy, the onset of interband transitions shifts significantly from ≈500 nm in pure Au to ≈315 nm for pure Ag unlike what happens for the mixing rule; and second, in the near-IR region for the alloy, there is a non-linear behavior in the real part of the refractive index that leads to values of n larger than those for pure metals. The physical reason for the presence of this shift is the variation of the number density of the minority constituent of the material. Since such atoms act as scattering centers, a variation in the resistivity of the material and, ultimately, in the damping constant is induced. The damping constant reaches its maximum value for the composition Ag 50% −Au 50%.[41] The non-linear behavior at near IR is caused by the difference in electronegativity between Ag and Au, resulting in a considerable transfer of electronic density from Ag to Au. This charge transfer stresses and modifies the lattice, producing an additional damping.

In Figure 8, we report the normalized experimental UV−Vis absorbance in good agreement with the calculated values for the re-irradiated mixtures with different compositions. For the simulated absorbance, we adopted the previously discussed model for the dielectric constant of the alloy, and also in this case, we considered a log normal distribution in size (see eqs 1111 and 12). In Table 3, we report the parameters obtained in the best fit procedure. We underline that, as a secondary effect of the re-irradiation procedure, the obtained colloids undergo a further NP fragmentation so that a narrower size distribution results as compared to that used for the best fit of Figure 3.

The high-magnification TEM observations that we performed on the re-irradiated r-$Ag_{50}Au_{50}$ sample, the details of which we discussed in the section Synthesis and Characterization of the Colloids (Figure 2d−f), provide further experimental support that laser re-irradiation results in the formation of NPs of Ag−Au alloys.

https://dx.doi.org/10.1021/acs.jpcc.0c05270
J. Phys. Chem. C 2020, 124, 24930−24939

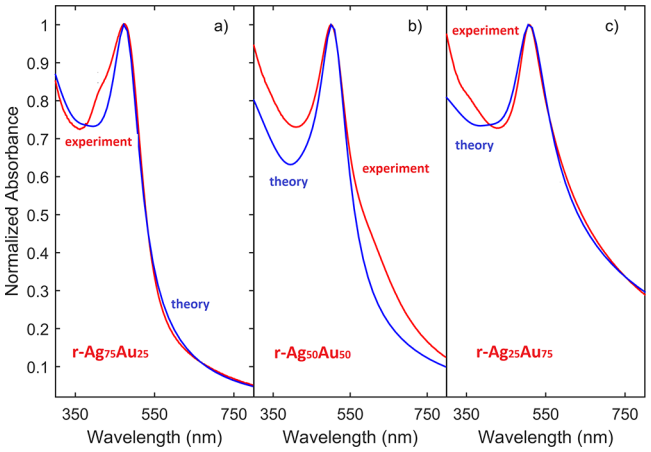

Figure 8. Experimental (red line) and calculated (blue line) normalized extinction spectra of re-irradiated colloids of different compositions: (a) r-$Ag_{75}Au_{25}$; (b) r-$Ag_{50}Au_{50}$; (c) r-$Ag_{25}Au_{75}$.

Table 3. Values of the Parameters Obtained through the Best Fit Procedure of the Experimental Data Shown in Figure 8

	r_{av} (nm)	σ	r_{min} (nm)	r_{max} (nm)
25%Au−75%Ag	10	2	1	100
50%Au−50%Ag	10	2	1	100
75%Au−25%Ag	10	2.5	1	100

CONCLUSIONS

We introduced a theoretical approach that makes use of the complete theory of scattering to accurately describe light absorption in AgAu alloyed NPs. We tested the results of our analysis to interpret the features of the extinction spectra collected from colloids synthesized by PLAL, covering a broad composition range. Provided it is fed with the optical constants of other alloys over the compositional range of interest, our approach allows for designing the SPR as a function of the main process parameters, namely, the composition of the mechanical mixture leading to the alloy and the average size of the constituent NPs.

AUTHOR INFORMATION

Corresponding Author

Paolo Maria Ossi − *Dipartimento di Energia, Politecnico di Milano, 20133 Milano, Italy*; Phone: +39 02 2399 6319; Email: paolo.ossi@polimi.it.

Authors

Enza Fazio − *Dipartimento di Scienze Matematiche e Informatiche, Scienze Fisiche e Scienze della Terra, Università degli Studi di Messina, 98166 Messina, Italy*

Rosalba Saija − *Dipartimento di Scienze Matematiche e Informatiche, Scienze Fisiche e Scienze della Terra, Università degli Studi di Messina, 98166 Messina, Italy*

Marco Santoro − *Dipartimento di Scienze Matematiche e Informatiche, Scienze Fisiche e Scienze della Terra, Università degli Studi di Messina, 98166 Messina, Italy*

Saidi Abir − *Dipartimento di Scienze Matematiche e Informatiche, Scienze Fisiche e Scienze della Terra, Università degli Studi di Messina, 98166 Messina, Italy*

Fortunato Neri − *Dipartimento di Scienze Matematiche e Informatiche, Scienze Fisiche e Scienze della Terra, Università degli Studi di Messina, 98166 Messina, Italy*

Matteo Tommasini − *Dipartimento di Chimica, Materiali e Ingegneria Chimica "G. Natta", Politecnico di Milano, 20133 Milano, Italy*; orcid.org/0000-0002-7917-426X

Complete contact information is available at: https://pubs.acs.org/10.1021/acs.jpcc.0c05270

Notes

The authors declare no competing financial interest.

ADDITIONAL NOTE

[1]The codes used in support of the findings of this study follow the analytical approach described in ref 22. They are available from the authors upon reasonable request.

REFERENCES

(1) Mesch, M.; Metzger, B.; Hentschel, M.; Giessen, H. Nonlinear Plasmonic Sensing. *Nano Lett.* **2016**, *16*, 3155−3159.

(2) Poletti, A.; Fracasso, G.; Conti, G.; Pilot, R.; Amendola, V. Laser generated gold nanocorals with broadband plasmon absorption for photothermal applications. *Nanoscale* **2015**, *7*, 13702−13714.

(3) Burrows, N. D.; Harvey, S.; Idesis, F. A.; Murphy, C. J. Understanding the SeedMediated Growth of Gold Nanorods through a Fractional Factorial Design of Experiments. *Langmuir* **2017**, *33*, 1891−1907.

(4) Valsecchi, C.; Brolo, A. G. Periodic metallic nanostructures as plasmonic chemical sensors. *Langmuir* **2013**, *29*, 5638−5649.

(5) Jafarkhani, P.; Torkamany, M. J.; Dadras, S.; Chehrghani, A.; Sabbaghzadeh, J. Necklace-shaped Au−Ag nanoalloys: laser-assisted synthesis and nonlinear optical properties. *Nanotechnology* **2011**, *22*, 235703.

(6) Galopin, E.; Barbillat, J.; Coffinier, Y.; Szunerits, S.; Patriarche, G.; Boukherroub, R. Silicon Nanowires Coated with Silver Nanostructures as Ultrasensitive Interfaces for Surface-Enhanced Raman Spectroscopy. *ACS Appl. Mater. Interfaces* **2009**, *1*, 1396−1403.

(7) D'Andrea, C.; Faro, M. J. L.; Bertino, G.; Ossi, P. M.; Neri, F.; Trusso, S.; Musumeci, P.; Galli, M.; Cioffi, N.; Irrera, A.; et al. Decoration of silicon nanowires with silver nanoparticles for ultrasensitive surface enhanced Raman scattering. *Nanotechnology* **2016**, *27*, 375603.

(8) Ossi, P. M.; Bailini, A. Cluster growth in an ablation plume propagating through a buffer gas. *Appl. Phys. A: Mater. Sci. Process.* **2008**, *93*, 645−650.

(9) Neri, F.; Ossi, P. M.; Trusso, S. Cluster synthesis and assembling in laser-generated plasmas. *Riv. Nuovo Cimento* **2011**, 103−149.

(10) Amendola, V.; Meneghetti, M. Laser ablation synthesis in solution and size manipulation of noble metal nanoparticles. *Phys. Chem. Chem. Phys.* **2009**, *11*, 3805−3821.

(11) Dell'Aglio, M.; Mangini, V.; Valenza, G.; De Pascale, O.; De Stradis, A.; Natile, G.; Arnesano, F.; De Giacomo, A. Silver and gold nanoparticles produced by pulsed laser ablation in liquid to investigate their interaction with Ubiquitin. *Appl. Surf. Sci.* **2016**, *374*, 297−304.

(12) Tommasini, M.; Zanchi, C.; Lucotti, A.; Bombelli, A.; Villa, N. S.; Casazza, M.; Ciusani, E.; De Grazia, U.; Santoro, M.; Fazio, E.; et al. Laser-synthesized SERS substrates as sensors toward therapeutic drug monitoring. *Nanomaterials* **2019**, *9*, 677.

(13) Izgaliev, A. T.; Simakin, A. V.; Shafeev, G. A.; Bozon-Verduraz, F. Intermediate phase upon alloying Au-Ag nanoparticles under laser exposure of the mixture of individual colloids. *Chem. Phys. Lett.* **2004**, *390*, 467−471.

(14) Compagnini, G.; Messina, E.; Puglisi, O.; Nicolosi, V. Laser synthesis of Au/Ag colloidal nano-alloys: Optical properties, structure and composition. *Appl. Surf. Sci.* **2007**, *254*, 1007−1011.

(15) Hajiesmaeilbaigi, F.; Motamedi, A. Synthesis of Au/Ag Alloy nanoparticles by Nd: YAG laser irradiation. *Laser Phys. Lett.* **2007**, *4*, 133−137.
(16) Papagiannouli, I.; Aloukos, P.; Rioux, D.; Meunier, M.; Couris, S. Effect of the composition on the nonlinear optical response of Au_xAg_{1-x} nano-alloys. *J. Phys. Chem. C* **2015**, *119*, 6861−6872.
(17) Besner, S.; Meunier, M. Femtosecond laser synthesis of AuAg nanoalloys: Photoinduced oxidation and ions release. *J. Phys. Chem. C* **2010**, *114*, 10403−10409.
(18) Compagnini, G.; Messina, E.; Puglisi, O.; Cataliotti, R. S.; Nicolosi, V. Spectroscopic evidence of a core-shell structure in the earlier formation stages of Au-Ag nanoparticles by pulsed laser ablation in water. *Chem. Phys. Lett.* **2008**, *457*, 386−390.
(19) Gong, C.; Leite, M. S. Noble Metal Alloys for Plasmonics. *ACS Photonics* **2016**, *3*, 507−513.
(20) Rioux, D.; Vallières, S.; Besner, S.; Muñoz, P.; Mazur, E.; Meunier, M. An analytic model for the dielectric function of Au, Ag, and their Alloys. *Adv. Opt. Mater.* **2014**, *2*, 176−182.
(21) Peña-Rodríguez, O.; Caro, M.; Rivera, A.; Olivares, J.; Perlado, J. M.; Caro, A. Optical properties of Au-Ag alloys: An ellipsometric study. *Opt. Mater. Express* **2014**, *4*, 403−410.
(22) Borghese, F.; Denti, P.; Saija, R. *Scattering from Model Nonspherical Particles: Theory and Applications to Environmental Physics*; Springer-Verlag: Berlin and Heidelberg GmbH & Co. KG: 2010.
(23) Waterman, P. C. Symmetry, Unitarity, and Geometry in Electromagnetic Scattering. *Phys. Rev. D* **1971**, *3*, 825−839.
(24) Jackson, J. D. *Classical electrodynamics*, 3rd ed.; Wiley: New York, NY, 1999.
(25) Mie, G. Beiträge zur Optik trüber Medien, speziell kolloidaler Metallösungen. *Ann. Phys.* **1908**, *330*, 377−445.
(26) Saija, R.; Iatì, M. A.; Denti, P.; Borghese, F.; Giusto, A.; Sindoni, O. I. Efficient light-scattering calculations for aggregates of large spheres. *Appl. Opt.* **2003**, *42*, 2785−2793.
(27) Borghese, F.; Denti, P.; Saija, R.; Toscano, G.; Sindoni, O. I. Extinction coefficients for a random dispersion of small stratified spheres and a random dispersion of their binary aggregates. *J. Opt. Soc. Am. A* **1987**, *4*, 1984−1991.
(28) Borghese, F.; Denti, P.; Saija, R.; Iatì, M. A.; Sindoni, O. I. Optical properties of a dispersion of anisotropic particles with non-randomly distributed orientations. The case of atmospheric ice crystals. *J. Quant. Spectrosc. Radiat. Transfer* **2001**, *70*, 237−251.
(29) Buffat, P.-A.; Flüeli, M.; Spycher, R.; Stadelmann, P.; Borel, J.-P. Crystallographic structure of small gold particles studied by high-resolution electron microscopy. *Faraday Discuss.* **1991**, *92*, 173−187.
(30) Yang, C.; Ma, L.; Maley, J.; Sammynaiken, R.; Feng, R.; Xiang, G.; Chen, W. Photoluminescence and X-Ray Excited Luminescence from Glutathione-Stabilized Gold Nanoparticles. *J. Biomed. Nanotechnol.* **2013**, *9*, 1827−1836.
(31) McKeehan, L. W. The Crystal Structure of Silver-Palladium and Silver-Gold Alloys. *Phys. Rev.* **1922**, *20*, 424−432.
(32) Letzel, A.; Santoro, M.; Frohleiks, J.; Ziefuß, A. R.; Reich, S.; Plech, A.; Fazio, E.; Neri, F.; Barcikowski, S.; Gökce, B. How the re-irradiation of a single ablation spot affects cavitation bubble dynamics and nanoparticles properties in laser ablation in liquids. *Appl. Surf. Sci.* **2019**, *473*, 828−837.
(33) Hupfeld, T.; Stein, F.; Barcikowski, S.; Gökce, B.; Wiedwald, U. Manipulation of the Size and Phase Composition of Yttrium Iron Garnet Nanoparticles by Pulsed Laser Post-Processing in Liquid. *Molecules* **2020**, *25*, 1869.
(34) Ziefuß, A. R.; Reichenberger, S.; Rehbock, C.; Chakraborty, I.; Gharib, M.; Parak, W. J.; Barcikowski, S. Laser Fragmentation of Colloidal Gold Nanoparticles with High-Intensity Nanosecond Pulses is Driven by a Single-Step Fragmentation Mechanism with a Defined Educt Particle-Size Threshold. *J. Phys. Chem. C* **2018**, *122*, 22125−22136.
(35) Johnson, P. B.; Christy, R. W. Optical Constants of the Noble Metals. *Phys. Rev. B* **1972**, *6*, 4370−4379.
(36) Vinod, M.; Gopchandran, K. G. Au, Ag and Au:Ag colloidal nanoparticles synthesized by pulsed laser ablation as SERS substrates. *Prog. Nat. Sci.: Mater. Int.* **2014**, *24*, 569−578.
(37) Bishop, K. J. M.; Wilmer, C. E.; Soh, S.; Grzybowski, B. A. Nanoscale Forces and Their Uses in Self-Assembly. *Small* **2009**, *5*, 1600−1630.
(38) Jain, P. K.; El-Sayed, M. A. Plasmonic coupling in noble metal nanostructures. *Chem. Phys. Lett.* **2010**, *487*, 153−164.
(39) Aspnes, D. E.; Theeten, J. B.; Hottier, F. Investigation of effective-medium models of microscopic surface roughness by spectroscopic ellipsometry. *Phys. Rev. B* **1979**, *20*, 3292−3302.
(40) Johs, B.; Hale, J. S. Dielectric function representation by B-splines. *Phys. Status Solidi A* **2008**, *205*, 715−719.
(41) Nishijima, Y.; Akiyama, S. Unusual optical properties of the Au/Ag alloy at the matching mole fraction. *Opt. Mater. Express* **2012**, *2*, 1226−1235.

https://dx.doi.org/10.1021/acs.jpcc.0c05270
J. Phys. Chem. C 2020, 124, 24930−24939